

# Loss Estimation of a Dual Active Bridge as part of a Solid State Transformer using Frequency Domain Modelling

Nikolas Menger

Elektrotechnisches Institut (ETI)  
 Karlsruhe Institute of Technology (KIT)  
 Karlsruhe, Germany  
 nikolas.menger@kit.edu

Tobias Merz

Elektrotechnisches Institut (ETI)  
 Karlsruhe Institute of Technology (KIT)  
 Karlsruhe, Germany  
 tobias.merz@kit.edu

Jannik Gehring

Elektrotechnisches Institut (ETI)  
 Karlsruhe Institute of Technology (KIT)  
 Karlsruhe, Germany

Fabian Sommer

Elektrotechnisches Institut (ETI)  
 Karlsruhe Institute of Technology (KIT)  
 Karlsruhe, Germany  
 fabian.sommer@kit.edu

Marc Hiller

Elektrotechnisches Institut (ETI)  
 Karlsruhe Institute of Technology (KIT)  
 Karlsruhe, Germany  
 marc.hiller@kit.edu

**Abstract**—This paper proposes an improved method for the loss estimation of a Dual Active Bridge (DAB) using frequency domain modelling. The method uses a detailed, frequency depending transformer model to describe even highly utilized DABs. The model is used to estimate the occurring losses of a DAB as part of an modular Solid State Transformer (SST). The influence of the SST's phase power ripple is considered for the loss estimation. The results of the frequency domain model and the loss calculation are validated using measurement data of an SST-cell prototype.

**Index Terms**—Solid-State Transformer, Analytical losses computation, Cascaded H-Bridge, Dual Active Bridge (DAB)

## I. INTRODUCTION

Solid State Transformers (SST) are widely reported in the literature for various applications, for example as a replacement for conventional Line Frequency Transformers (LFT), smart-grids, renewable energy sources and data centers. SST utilize one or more Medium Frequency Transformers (MFT) interfaced by power electronic circuits and provide galvanic isolation, while offering advantages such as reactive power compensation, voltage regulation, harmonic filtering and power flow control [1]. In this paper an SST for interfacing a Direct Current (DC) microgrid with the Medium Voltage Alternating Current (MVAC) grid is considered. The two-stage topology shown in Fig. 1a was proposed in [2] and is based on a three phase Cascaded H-Bridge (CHB) converter in star connection. Each of the series connected CHB cells shown in Fig. 1b consists of a full bridge on the AC side for AC-DC conversion and a Dual Active Bridge (DAB) to provide the galvanic isolation to the DC side.

This paper will focus on the topology-induced cell power ripple and its impact on the power loss of the DAB. The paper is structured as follows: Firstly the cell power

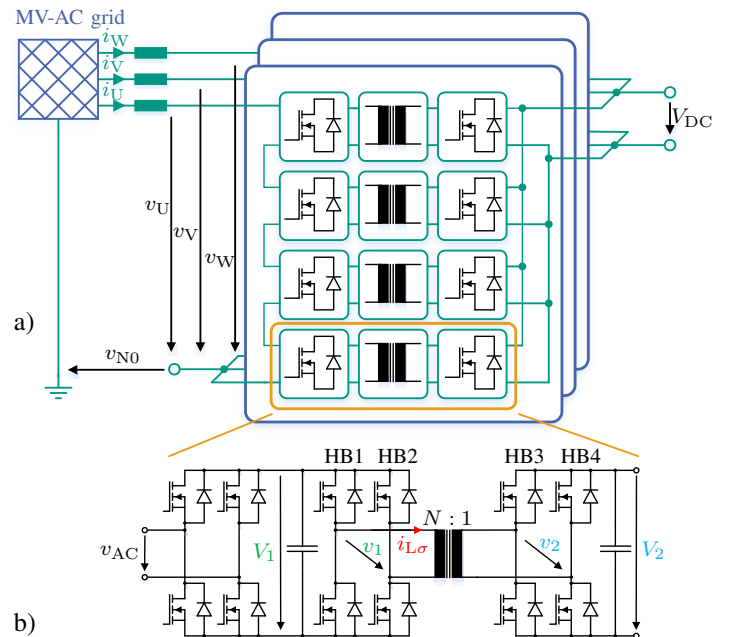


Fig. 1: Structure of the modular SST and cell topology

of the SST is explained. Subsequent, a methodology for the calculation of the voltage and current waveforms of the DAB is proposed. Afterwards, a loss estimation of the DAB for constant power operation is presented. The proposed methods are validated using measurement data of a scaled low voltage SST-cell prototype. In the end, the impact of the cell power ripple on the converter efficiency is analyzed.

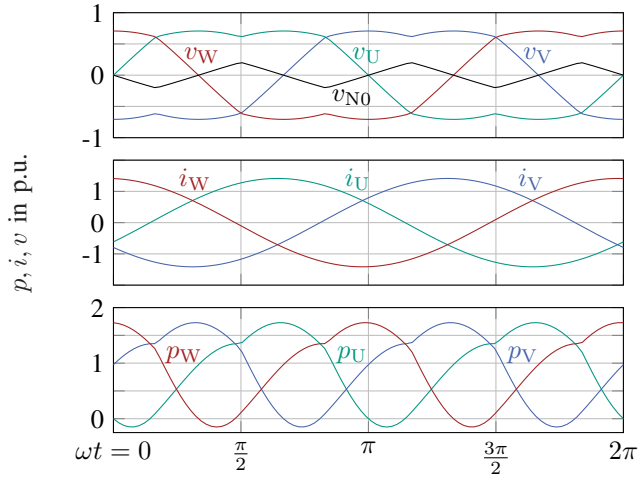


Fig. 2: Idealized AC-side voltages, currents and output power of the SST

## II. SST CELL POWER RIPPLE

For a CHB connected to a 50 Hz grid, the output power of each phase is fluctuating with 100 Hz. The power ripple can be reduced injecting a zero voltage component  $v_{N0}$ . However, the remaining ripple has to be either buffered by the DC-link capacitors, requiring bulky capacitors to keep the cell voltage ripple in an acceptable region, or supplied by the DAB. In the latter case, the DAB is operated with continuously changing setpoints to maintain a constant output voltage of the DC-link capacitors.

The analysis of the cell power ripple is simplified by assuming the idealized sinusoidal current and voltage waveform of a three-phase, symmetric AC grid and an equal distribution of the phase power among all cells within a phase. A triangular zero voltage component  $v_{N0}$  with triple grid frequency is used to increase the maximum output voltage of the CHB [3]. Figure 2 shows the normalized and idealized phase voltages  $v$ , grid currents  $i$  and phase power  $p$  of the CHB for a single AC-grid period at rated output power with  $\cos(\varphi_c) = 0.9_{\text{ind}}$ . In this case, the instantaneous power is periodically changing with sections of negative power. If an equal power distribution between all SST-cells within a phase is assumed, the instantaneous power of a cell in phase U can be described by

$$p(t) = \frac{v_U i_U}{m} = \frac{\hat{v} \hat{i}}{2m} [\cos(\varphi_c) - \cos(2\omega_g t + \varphi_c) + \frac{4 \sin(\omega_g t + \varphi_c)}{\pi^2} \cdot \sum_{n=1}^{\infty} \frac{\cos((2n-1)(\omega_g t + \frac{\pi}{2}))}{(2n-1)^2}] \quad (1)$$

where  $\hat{v}$  and  $\hat{i}$  are the amplitudes of the grid voltage and current,  $\varphi_c$  is the phase displacement between the voltage and the grid current,  $\omega_g = 2\pi f_g$  is the angular grid frequency and  $m$  is the number of cells per phase. The remaining phases V and W have an identical waveform, shifted by  $\frac{2\pi}{3}$  and  $\frac{4\pi}{3}$ , respectively.

## III. FREQUENCY DOMAIN MODELLING OF THE DUAL ACTIVE BRIDGE

The DAB is a galvanic isolated, bidirectional DC-DC converter. It consists of two full bridges, connected by a MFT. The advantages of the DAB include high power density, good component utilization and high efficiency due to soft switching [4].

Usually, the DAB is modelled in the time domain. There, the two full bridges can be replaced by ideal, rectangular voltage sources. In many cases, the MFT is modelled only by its stray inductance. While this model is sufficient to explain the basic operation and derive simple modulation schemes, it can become inaccurate for high-power or highly utilized DAB converters, where winding resistances or a finite magnetizing inductance can strongly influence the behavior. Therefore, more complex MFT-models are employed, which include a finite magnetizing inductance, employ a lossy transformer model [5] or include intra- and inter-winding capacitances [6].

If the MFT is modelled only by its stray inductance, the voltage and current waveforms of the DAB can be easily calculated for simple modulation schemes such as Single Phase Shift (SPS) or Triangular Current Mode (TCM). In these cases, the rectangular voltage waveforms will lead to a piecewise linear current waveform. For lossy transformer models, the current waveforms can be described by piecewise exponential functions. For even more complex models including capacitances, the differential equations of the circuit need to be solved, which makes the calculation even more complicated. Time-domain modelling also leads to a complex distinction of cases if sophisticated modulation schemes are employed [7].

To overcome these drawbacks, Frequency Domain Modelling (FDM) was proposed to allow for easy calculation of the current and voltage waveforms of a DAB for arbitrary modulation schemes, even if a detailed transformer model is used [8], [9]. FDM was proposed for the three-phase DAB in [10]. It can be used to calculate optimized modulation schemes, which reduce the circulation current of the transformer [11], [12] or extend the Zero Voltage Switching (ZVS)-region [9], [12]. In [13], FDM was used to optimize the magnetizing inductance to extend the ZVS-region.

In this paper, FDM is used to estimate the losses of the DAB. The equivalent circuit of the DAB, which is considered in this paper, is shown in Fig. 3. The two full bridges of the DAB are modelled using ideal, rectangular voltage sources. The transient behavior of the semiconductors, including the switching losses and commutation process, is neglected for the calculation of the waveforms. The coupling network between the two full bridges is modelled as a lossy T-equivalent circuit, which consists of the series resistances  $R_{s1,\nu}$ ,  $R_{s2,\nu}$ , the series inductances  $L_{s1,\nu}$ ,  $L_{s2,\nu}$  in combination with parallel path  $R_{\text{mag}}$  and  $L_{\text{mag}}$ . The frequency depending coupling network includes properties of the MFT, the semiconductor devices, the DC-link capacitances and the layout of the Printed Circuit Board (PCB). It is assumed that the MFT is operated in the

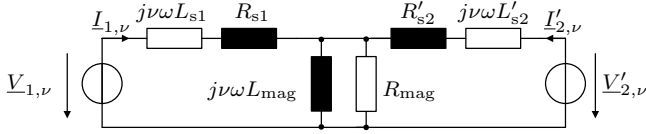


Fig. 3: Equivalent circuit model of the DAB in the frequency domain

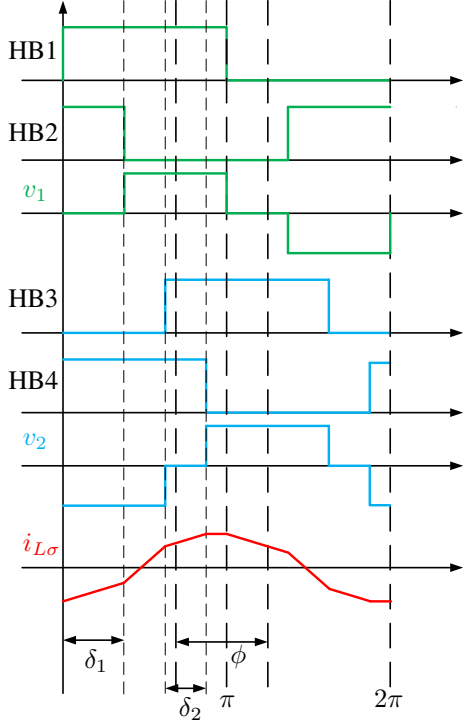


Fig. 4: Phase-Shift definitions of the DAB

linear region, where hysteresis and saturation can be neglected. The parametrization of the model is presented in Section V.

The waveforms of the converter are described in the frequency domain using Fourier series, where a real, periodic signal  $x(t)$  can be described using

$$x(t) = \sqrt{2} \cdot \sum_{m=0}^{\infty} \underline{C}_\nu \cdot e^{j\nu\omega t} \quad (2)$$

where  $\omega = 2\pi f_{sw}$  is the fundamental angular frequency and  $\underline{C}_\nu$  are the complex Fourier coefficients. The full bridges are replaced by rectangular voltage sources, whose complex Fourier coefficients  $\underline{V}_{1,\nu}$  and  $\underline{V}_{2,\nu}$  are given by

$$\underline{V}_{1,\nu} = \frac{2\sqrt{2}V_1}{\nu\pi} \sin\left(\nu\frac{\pi - \delta_1}{2}\right), \nu = 1, 3, 5, \dots M \quad (3)$$

$$\underline{V}_{2,\nu} = \frac{2\sqrt{2}V_2}{\nu\pi} \sin\left(\nu\frac{\pi - \delta_2}{2}\right) e^{-j\nu\phi}, \nu = 1, 3, 5, \dots M \quad (4)$$

where  $V_1$  and  $V_2$  are the DC-link voltages,  $\phi$ ,  $\delta_1$ ,  $\delta_2$  are the phase shift angles and  $M$  is the ordinal of the highest considered harmonic. The definitions of  $\phi$ ,  $\delta_1$  and  $\delta_2$  are shown in Fig. 4. The phase shift  $\phi$ , which describes a displacement of

the secondary side voltage waveform results in the modulation  $e^{-j\nu\phi}$  in the Fourier domain.  $\delta_1$  and  $\delta_2$  describe the phase shift between the two half bridges of each side of the DAB, resulting in time segments of zero voltage in  $v_1$  and  $v_2$  respectively, as shown in Fig. 4. In the Fourier domain, this leads to a reduction of the Fourier coefficients amplitudes. To obtain the currents of the DAB, the superposition principle is employed. Therefore, the currents of both voltage sources can be calculated independently. The Fourier spectra of the source currents are described by

$$\underline{I}_{q1,\nu} = \frac{2\sqrt{2}V_1}{\nu\pi \cdot (\underline{Z}_{1,\nu} + \underline{Z}'_{2,\nu} \parallel \underline{Z}_{mag})} \sin\left(\nu\frac{\pi - \delta_1}{2}\right) \quad (5)$$

$$\underline{I}'_{q2,\nu} = \frac{2\sqrt{2}V_2}{\nu\pi \cdot (\underline{Z}'_{2,\nu} + \underline{Z}_{1,\nu} \parallel \underline{Z}_{mag})} \sin\left(\nu\frac{\pi - \delta_2}{2}\right) e^{-j\nu\phi} \quad (6)$$

where the frequency dependent circuit impedances  $\underline{Z}_{1,\nu}$ ,  $\underline{Z}'_{2,\nu}$  and  $\underline{Z}_{mag}$  are given by:

$$\underline{Z}_{1,\nu} = R_{s1,\nu} + j\nu\omega L_{s1,\nu} \quad (7)$$

$$\underline{Z}'_{2,\nu} = R'_{s2,\nu} + j\nu\omega L'_{s2,\nu} \quad (8)$$

$$\underline{Z}_{mag,\nu} = \frac{j\nu\omega R_{mag} L_{mag}}{R_{mag} + j\nu\omega L_{mag}} \quad (9)$$

The superposition of the source currents leads to the occurring transformer currents

$$\underline{I}_{1,\nu} = \underline{I}_{q1,\nu} - \frac{\underline{Z}_{mag,\nu}}{\underline{Z}_{1,\nu} + \underline{Z}_{mag,\nu}} \underline{I}'_{q2,\nu} \quad (10)$$

$$\underline{I}'_{2,\nu} = \underline{I}'_{q2,\nu} - \frac{\underline{Z}_{mag,\nu}}{\underline{Z}'_{2,\nu} + \underline{Z}_{mag,\nu}} \underline{I}_{q1,\nu} \quad (11)$$

If the voltage or current waveforms are required in the time domain, the calculation is either possible using the Fourier synthesis in (2) or using a Fast Fourier Transform (FFT)-algorithm, which enables a shorter computation time.

#### IV. DUAL ACTIVE BRIDGE LOSS ESTIMATION

The loss estimation of the DAB is done using the resulting waveforms of the FDM model. The estimation includes conduction losses and switching losses of the MOSFETs as well as copper losses and core loss of the transformer. The model neglects losses of the DC-link capacitors and the power consumption of the control and gate-drive circuits.

##### A. Conduction losses

The conduction and copper losses  $P_{c,k}$  are calculated in the Fourier spectrum with

$$P_{c,k} = \sum_{\nu=1}^M R_{sk,\nu} \underline{I}_{k,\nu} \underline{I}_{k,\nu}^* \quad (12)$$

where  $k = 1, 2$  denotes the transformer side. the frequency dependent resistance  $R_{sk,\nu}$  enables the consideration of current displacement effects due to skin and proximity effects inside the transformer windings or in the PCB traces. The calculation

is performed for both transformer sides with  $R_{s1,\nu}, R_{s2,\nu}$  and  $\underline{L}_{1,\nu}, \underline{L}_{2,\nu}$ , respectively. For a loss separation between MOSFET and transformer conduction losses, (12) can be calculated for each component independently.

### B. Switching losses

The switching process of the MOSFET produces losses, which can contribute a significant amount to the MOSFET's total losses, especially for high switching frequencies  $f_{sw}$ . The switching losses are depending on several parameters, including the junction temperature  $T_j$ , parasitic elements of the MOSFET and the peripheral circuit, the drain current  $i_D$  and the drain-source voltage  $v_{DS}$  [14]. The switching losses are reduced if soft switching is apparent. For the DAB, ZVS and Zero Current Switching (ZCS) are possible soft switching entities. ZCS occurs if the MOSFET is turned off with no current flowing through the semiconductor, therefore significantly reducing the turn-off loss. For the DAB, ZCS occurs mainly for modulation schemes similar to TCM, where one or more switching events occur at zero current. ZVS takes place when the freewheeling diode of the MOSFET is conducting prior to the turn-on of the MOSFET. This significantly reduces the turn-on losses, since the MOSFET is turned-on with only the diode's forward voltage being apparent. To achieve ZVS, the output capacitance of the MOSFETs needs to be discharged by the transformer current during the blocking time of the half bridge, which represents a transfer of reactive energy from the inductive elements in the transformer to the MOSFET's output capacitances. Several ZVS boundary conditions have been discussed in the literature. A very simple approach is based on the MOSFET's current direction, which assumes that a negative current leads to a ZVS turn-on [15]. More sophisticated methods compare the energy of the inductor with the required energy of the electrical field in the MOSFETs output capacitance [16] or model the commutation process in the time-domain [17]. However, due to the low complexity, this paper will use the simple current direction based approach.

For hard switching, the total switching loss of a single MOSFET are calculated using

$$P_{M,sw} = f_{sw} \cdot (E_{on}(v_{DS}, i_D, T_j) + E_{off}(v_{DS}, i_D, T_j)) \quad (13)$$

where  $E_{on}(v_{DS}, i_D, T_j)$  and  $E_{off}(v_{DS}, i_D, T_j)$  are the turn-on and turn-off energies, which are either given in the manufacturers datasheet or can be obtained by performing double-pulse measurements [20]. Since the switching losses is dependent on the apparent current during the switching event, the time-domain waveform needs to be calculated from the Fourier domain. If the ZVS condition is satisfied, it is assumed that the MOSFET's turn-on is lossless ( $E_{on} = 0$ ), therefore (13) is simplified to

$$P_{M,switch} = f_{sw} \cdot E_{off}(v_{DS}, i_D, T_j) \quad (14)$$

### C. Core loss

The core losses of inductive components in power electronic applications are often estimated using extended versions of

the Steinmetz equation, which was originally formulated to calculate the per unit power loss for a sinusoidal excitation using

$$p_v = k \cdot f^\alpha \cdot B^\beta \quad (15)$$

where  $k$ ,  $\alpha$  and  $\beta$  are the empirically derived, material dependent Steinmetz parameters [18]. The so-called Original Steinmetz Equation (OSE) was improved in order to allow the loss estimation for non-sinusoidal excitation using the Steinmetz parameters. The resulting improved Generalized Steinmetz Equation (iGSE) is formulated as

$$p_c = \frac{1}{T} \int_0^T k_1 \left| \frac{dB}{dt} \right|^\alpha (\Delta B)^{\beta-\alpha} dt \quad (16)$$

where  $B$  is the instantaneous core flux density,  $\Delta B$  is the peak-to-peak flux density [19].  $k_1$  is calculated from

$$k_1 = \frac{k}{(2\pi)^{\alpha-1} \int_0^{2\pi} |\cos \theta|^\alpha |\cos \theta|^{\beta-\alpha} d\theta} \quad (17)$$

The total core loss can be calculated by multiplying the per unit power loss with the total core volume  $V_{core}$ :

$$P_C = p_c V_{core} \quad (18)$$

For this paper, the excitation of the MFT is calculated as the voltage across the magnetizing inductance  $L_{mag}$ , which can be calculated in the Fourier domain from

$$\underline{V}_{e,\nu} = \underline{V}_{1,\nu} - \underline{Z}_{1,\nu} \underline{I}_{1,\nu} \quad (19)$$

In order to use (16), the time-domain representation of the excitation voltage  $v_e(t)$  needs to be calculated from the Fourier coefficients  $\underline{V}_{e,\nu}$ . From  $v_e(t)$ , the core's flux density  $B(t)$  is calculated using the relationship

$$v_e(t) = N A_{core} \frac{dB(t)}{dt} \quad (20)$$

where  $N$  is the number of turns of the primary side and  $A_{core}$  is the core's cross section.

### D. Loss estimation for SST operation

When used as the DC-DC converter of an SST-cell, the operation with fluctuating power influences the average losses of the DAB. To consider this behavior, the losses of the DAB are calculated independently for each operation point during the AC grid period using (1). This calculation method requires  $f_{sw} \gg f_g$ , so that the operation point of the DAB are changing only slightly between two switching periods, leading to a quasi-steady-state operation. In the following, this operation mode is called Fluctuating Power (FP) mode, while the operation with constant power is denoted Constant Power (CP) mode.

## V. MODEL PARAMETRIZATION

The frequency domain model and the loss estimation of the DAB are validated using a scaled prototype of an SST-cell, which is shown in Fig. 5. To obtain a sufficient accuracy for the loss estimation, the parameters of the relevant components need to be characterized in detail. For the DAB, the semiconductor devices and the transformer properties are the most relevant characteristics.



Fig. 5: Low voltage SST-cell prototype

TABLE I: Hardware Setup Parameter

Parameter	Primary Side	Secondary Side
Semiconductor	IPP026N10NF2S	G3R160MT12D
$V_{DS,max}$	100 V	1200 V
$I_{D,nom}$	184 A	19 A
$R_{DS,on}(25^\circ\text{C})$	2.3 m $\Omega$	160 m $\Omega$

### A. Semiconductor characterization

The MOSFETs on resistance  $R_{DS,on}$  as well as the switching energies  $E_{on}$  and  $E_{off}$  are important parameters for the loss calculation. Two different MOSFETs are used due to the different voltage levels on the primary and secondary side of the DAB. On the AC side of the SST cell, the silicon MOSFET IPP026N10NF2S is used. On the DC side, the silicon carbide MOSFET G3R160MT12D is used. The relevant datasheet values of the MOSFETs are shown in Table I. The datasheet of the G3R160MT12 MOSFET supplies detailed information on the switching energy under different working conditions. These data are not available for the IPP026N10NF2S MOSFET. Therefore, the switching energy is measured using a double-pulse test bench [20]. From these measurements, the switching energy for the turn-on event and the turn-off event can be calculated. The measurements are carried out for different drain-source voltages  $V_{DS}$  and different junction temperatures  $T_j$ . The results of the double-pulse tests are shown in Fig. 6 and Fig. 7, respectively. As expected, both turn-on energy  $E_{on}$  and turn-off energy  $E_{off}$  are increasing with rising current  $I_D$ , voltage  $V_{DS}$  and temperature  $T_j$ .

### B. MFT characterization

For the MFT, a frequency dependent model improves the calculation of the steady-state waveforms and enables the correct consideration of current displacement due to skin and proximity effect. The transformer has a winding ratio of  $n = 14.11$ . The equivalent circuit parameters of the MFT are estimated using a Keysight E4990A Impedance Analyzer. The magnetizing inductance  $L_{mag} = 1.67$  mH is constant in the relevant frequency region. The parallel core loss resistance  $R_{mag}$  has a much higher impedance and is neglected for the calculation of the waveform. The series resistances  $R_{s1}$  and  $R_{s2}$  show a significant frequency dependency, for the series

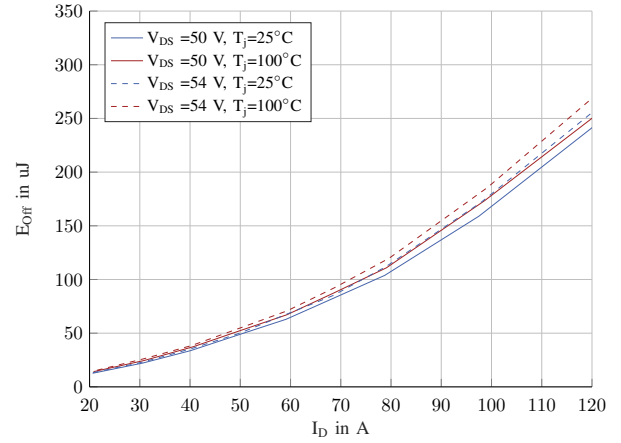


Fig. 6: Turn-off losses of the primary side MOSFETs

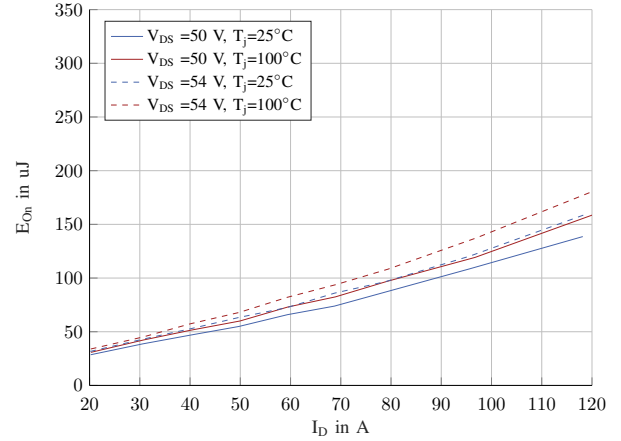


Fig. 7: Turn-on losses of the primary side MOSFETs

inductances  $L_{s1}$  and  $L_{s2}$  a small frequency dependency is apparent. The estimation result is shown in Fig. 8.

For the calculation of the core losses, the transformer's core parameters are relevant. A PM 74/59 core, made of N87 ferrite with  $N = 63.5$  turns is used. The core's cross section  $A_{core}$  and the core volume  $V_{core}$  are obtained from the datasheet [21], while the Steinmetz parameters for N87 ferrite are given in [22].

## VI. MEASUREMENT RESULTS

The model validation is split in three parts. First, the results of the frequency domain model are validated with measured steady-state waveforms. Subsequently, the loss estimation in CP-mode is validated with efficiency measurements. Eventually, the loss estimation for FP-mode is validated. The measurements are carried out at  $V_1 = 53$  V,  $V_2 = 750$  V and  $f_{sw} = 62.5$  kHz. SPS is used as the modulation scheme of the DAB.

### A. FDM validation

Figure 9 shows the current waveforms of the inductor currents  $i_1$  and  $i_2$ . The calculated waveform FDM<sub>1</sub> using the proposed transformer model from Fig. 3 with the parameters from Section V matches the measurement result with adequate

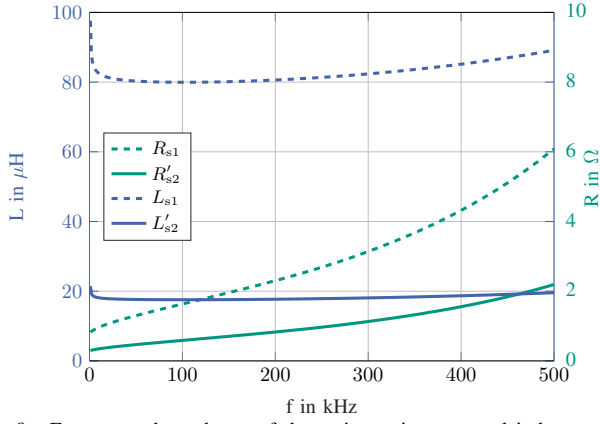


Fig. 8: Frequency dependency of the series resistances and inductances of the transformer

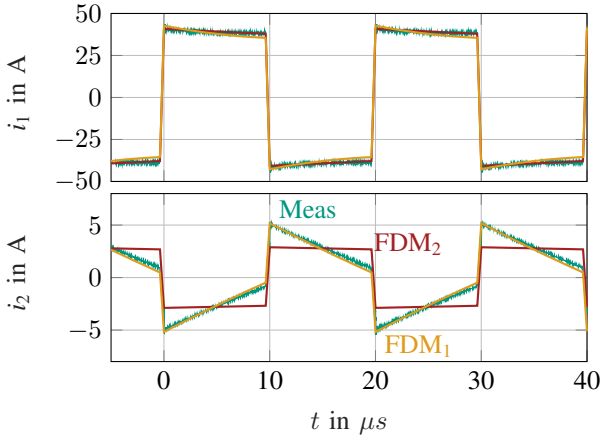


Fig. 9: Comparison of the FDM modelling using the T-equivalent circuit (FDM<sub>1</sub>) and a simple transformer model (FDM<sub>2</sub>) and measurements for SPS

accuracy. For a comparison, the calculation is also performed using a simple transformer model, only considering a series inductance. The resulting waveform using the simple transformer model (FDM<sub>2</sub>) differs significantly from the measurement data, indicating that the magnetizing inductance and the copper losses have a relevant impact on the resulting waveforms.

### B. Loss estimation for CP-operation

To calculate the power losses  $P_d$  of the DAB for different operating conditions, the input  $P_{in}$  and output power  $P_{out}$  of the DAB are measured using a power analyzer. The losses are then calculated using

$$P_d = P_{in} - P_{out} \quad (21)$$

The drawback of this measurement method is the required accuracy, which needs to be sufficiently high with respect to the power difference. The maximum measurement uncertainty is estimated using the datasheet parameters of the power analyzer [23] and the current transducers [24], assuming uncorrelated uncertainties. The resulting uncertainty is  $\pm 4.9$  W for the entire measurement range of  $\pm 3000$  W. The measurements were carried out at 25 °C.

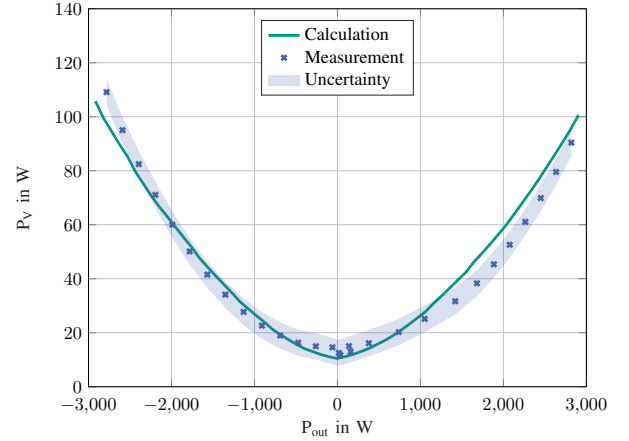


Fig. 10: Comparison of the calculated and measured losses of the scaled prototype

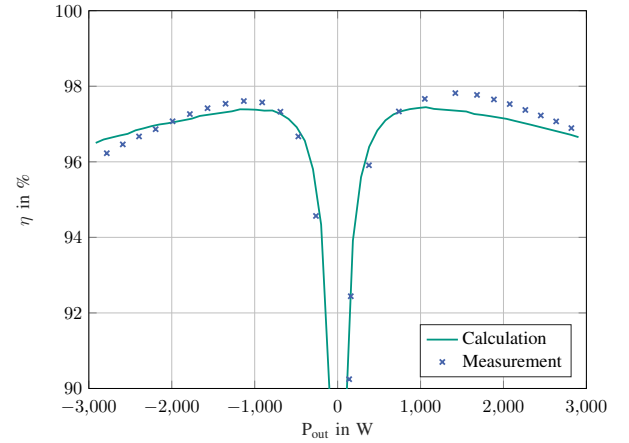


Fig. 11: Calculated and measured efficiency of the scaled prototype

The measured power dissipation  $P_d$  is shown in Fig. 10, together with the measurement uncertainty and the result of the loss estimation. For negative power transfer, the loss calculation corresponds with the measurement results within the measurement uncertainty. For higher negative power, the calculation underestimates the losses. For positive power transfer, the calculation overestimates the power dissipation of the DAB. This deviation could be caused by parameter inaccuracy, e.g. overestimated switching losses. The inaccuracy of the model is also visible in the efficiency curve of the DAB in Fig. 11. The efficiency curve shows that the considered DAB reaches the peak efficiencies of  $\eta = 97.9\%$  at 1200 W for positive power transfer and  $\eta = 97.6\%$  at  $-1200$  W for negative power transfer.

Fig. 12 shows the calculated losses of the SST-cell prototype, divided into the different loss mechanisms. For operation points with low power transfer, the dissipated power is dominated by the transformer's core losses and the semiconductor switching losses. With increasing power transfer, the percentage of the remaining loss components increases. For high power transfer, the transformer's copper losses become the dominating component of the losses. When comparing

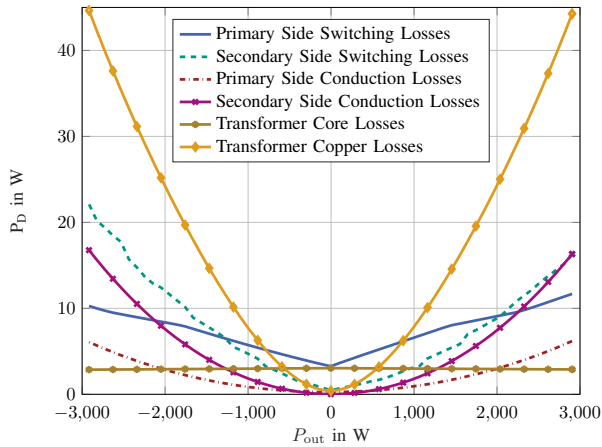


Fig. 12: Separation of the calculated loss components

positive and negative power transfer it is observed that the conduction losses of the semiconductors and the transformer are symmetric. In contrast, the switching losses show an asymmetrical behavior, which can be explained by the switching sequence of the semiconductors. For positive power transfer, the primary side switches prior to the secondary side. Due to influence of the magnetizing inductance, the primary side has a higher instantaneous current during the switching event, leading to higher switching losses. For negative power, this holds vice-versa.

### C. Loss estimation for FP-operation

As described in Section II, the DAB of the SST-cell operates with fluctuating power in order to reduce the necessary DC-link capacitor size. This operation mode has an impact on the dissipated power. Fig. 13 shows measurements of the operation with fluctuating power for different phase displacement angles  $\cos(\varphi_c)$ . All three operation points describe the behavior of a single SST-cell in a converter with  $m = 6$  cells per phase and the total power  $S = -25$  kVA. The measurements are carried out using a single SST-cell, which is supplied by two bidirectional power supplies. Due to the limited dynamic behavior of the power supplies, the measurement is carried out at a reduced grid frequency  $f_g = 5$  Hz. Fig. 14 shows the measured and calculated power dissipation for the described FP-operation. The calculation was done using the load profile from (1). The load profile was divided into  $16 \mu\text{s}$ -segments, which corresponds to the switching cycle of the DAB with  $f_{sw} = 62.5$  kHz. For these segments, the occurring power dissipation was calculated. For the continuous blue line, the calculation was performed using the FDM-model. For the dashed green line, the power dissipation was calculated by interpolation of the measurement results for the CP-operation shown in Fig. 9. For both cases, the mean power dissipation  $P_d$  was obtained by averaging the calculation results for the segments. It is observed that the loss estimation based on the CP-measurement results matches the measurement results closely, while the loss calculation based on the FDM-model shows an offset of 3 W. This inaccuracy corresponds to the

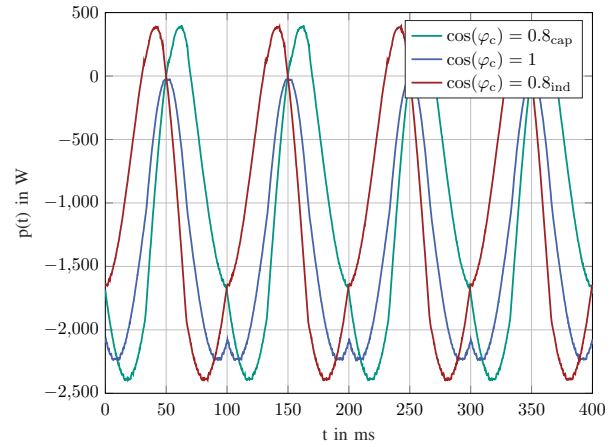


Fig. 13: Measurement of the power ripple of the DAB for FP-operation at  $S = -25$  kVA

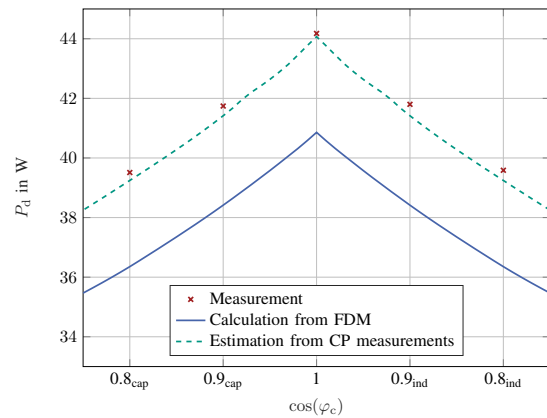


Fig. 14: Comparison of the measured losses for FP operation with the estimation results of the FDM model and a loss estimation based on the CP measurements

deviation of the FDM-model for the CP-operation shown in Fig. 9.

Fig. 15 depicts the expected loss increase of the FP operation in comparison to CP operation. The loss calculation is based on the CP measurement data. It is observed that the FP operation results in increased losses for the shown operation range. The loss increase results mainly from two factors. On the one hand, since the operation point is permanently changing, the DAB is not operating with its maximum efficiency. On the other hand, the DAB also has to transfer the reactive power that is provided to the AC grid, which results in increased losses for decreasing  $\cos(\varphi_c)$ . The influence of both factors would be reduced, if the DC-link capacitors were able to buffer the occurring power ripple. The increased losses from FP operation should be considered for the design of the power electronics and the cooling system.

## VII. CONCLUSION

This paper proposes a frequency domain based approach to calculate the voltage and current waveforms of a DAB. The calculated waveforms are used to estimate the converter

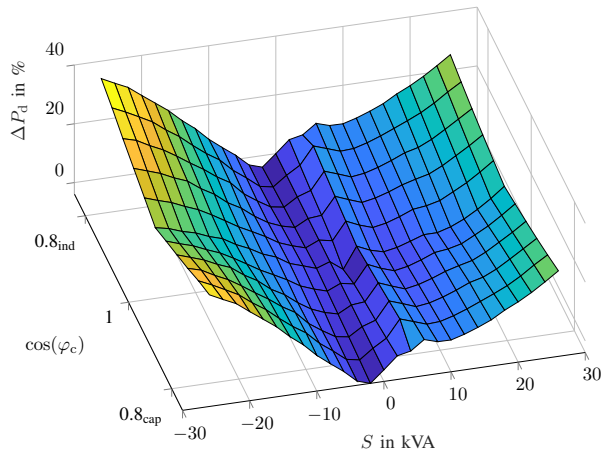


Fig. 15: Increased losses of the FP operation compared to CP operation

losses of the DAB, considering losses of the semiconductors and the transformer. The losses are estimated for constant power operation and fluctuating power operation. FP operation occurs, if the DAB is used as part of a CHB-based SST. It is shown that the FP operation can increase the losses of the DAB significantly. The measurement results validate the model in general, although small deviations between the model and the measurement are observed.

The model can be used in the detailed design process of an SST-cell. It is also possible to use the model in an offline-optimization in order to improve the efficiency of the SST.

#### REFERENCES

- [1] J. E. Huber and J. W. Kolar, "Solid-State Transformers," no. SEPTEMBER, 2016.
- [2] X. She, X. Yu, F. Wang, and A. Q. Huang, "Design and demonstration of a 3.6kV-120V/10KVA solid state transformer for smart grid application," *Conference Proceedings - IEEE Applied Power Electronics Conference and Exposition - APEC*, pp. 3429–3436, 2014. DOI: 10.1109/APEC.2014.6803801.
- [3] A. Tovaglieri, *Steuerverfahren für selbstgeführte Stromrichter*, 3. 2011, vol. 15, pp. 12–19, ISBN: 8610828378018. [Online]. Available: <https://doi.org/10.3929/ethz-a-010025751>.
- [4] W. A. A. D. Doncker and D. M. Divan, "A three-phase soft-switched high-power-density DC/DC converter for high-power applications," *IEEE Transactions on Industry Applications*, vol. 27, no. 1, pp. 63–73, 1991. DOI: 10.1109/28.67533.
- [5] F. Krismer and J. W. Kolar, "Accurate power loss model derivation of a high-current dual active bridge converter for an automotive application," *IEEE Transactions on Industrial Electronics*, vol. 57, no. 3, pp. 881–891, 2010, ISSN: 02780046. DOI: 10.1109/TIE.2009.2025284.
- [6] Z. Qin, Z. Shen, F. Blaabjerg, and P. Bauer, "Transformer Current Ringing in Dual Active Bridge Converters," *IEEE TRANSACTIONS ON INDUSTRIAL ELECTRONICS*, vol. 68, no. 12, pp. 12 130–12 140, 2021.
- [7] B. Liu, P. Davari, and F. Blaabjerg, "An Optimized Hybrid Modulation Scheme for Reducing Conduction Losses in Dual Active Bridge Converters," *IEEE Journal of Emerging and Selected Topics in Power Electronics*, vol. 9, no. 1, pp. 921–936, 2021, ISSN: 21686785. DOI: 10.1109/JESTPE.2019.2956323.
- [8] J. Everts, G. E. Sfakianakis, and E. A. Lomonova, "Using fourier series to derive optimal soft-switching modulation schemes for dual active bridge converters," *2015 IEEE Energy Conversion Congress and Exposition, ECCE 2015*, pp. 4648–4655, 2015. DOI: 10.1109/ECCE.2015.7310317.
- [9] J. Riedel, D. G. Holmes, C. Teixeira, and B. P. McGrath, "Harmonic-based determination of soft switching boundaries for 3-level modulated single-phase dual active bridge converters," *2015 IEEE Energy Conversion Congress and Exposition, ECCE 2015*, pp. 1505–1512, 2015. DOI: 10.1109/ECCE.2015.7309872.
- [10] J. Riedel, D. G. Holmes, B. P. McGrath, and C. Teixeira, "Determination of DC link harmonics in dual active bridge DC-DC converters using frequency domain analysis," *2016 IEEE 8th International Power Electronics and Motion Control Conference, IPEMC-ECCE Asia 2016*, pp. 70–77, 2016. DOI: 10.1109/IPEMC.2016.7512264.
- [11] B. Zhao, Q. Song, W. Liu, G. Liu, and Y. Zhao, "Universal High-Frequency-Link Characterization and Practical Fundamental-Optimal Strategy for Dual-Active-Bridge DC-DC Converter under PWM Plus Phase-Shift Control," *IEEE Transactions on Power Electronics*, vol. 30, no. 12, pp. 6488–6494, 2015, ISSN: 08858993. DOI: 10.1109/TPEL.2015.2430934.
- [12] J. Huang, Y. Wang, Z. Li, and W. Lei, "Unified Triple-Phase-Shift Control to Minimize Current Stress and Achieve Full Soft-Switching of Isolated Bidirectional DC-DC Converter," *IEEE Transactions on Industrial Electronics*, vol. 63, no. 7, pp. 4169–4179, 2016, ISSN: 02780046. DOI: 10.1109/TIE.2016.2543182.
- [13] J. Riedel, D. G. Holmes, B. P. McGrath, and C. Teixeira, "Maintaining Continuous ZVS Operation of a Dual Active Bridge by Reduced Coupling Transformers," *IEEE Transactions on Industrial Electronics*, vol. 65, no. 12, pp. 9438–9448, 2018, ISSN: 02780046. DOI: 10.1109/TIE.2018.2815993.
- [14] M. Rodríguez, A. Rodríguez, P. F. Miaja, D. G. Lamar, and J. S. Zúñiga, "An insight into the switching process of power MOSFETs: An improved analytical losses model," *IEEE Transactions on Power Electronics*, vol. 25, no. 6, pp. 1626–1640, 2010, ISSN: 08858993. DOI: 10.1109/TPEL.2010.2040852.
- [15] Y. Yan, H. Gui, and H. Bai, "Complete ZVS Analysis in Dual Active Bridge," *IEEE Transactions on Power Electronics*, vol. 36, no. 2, pp. 1247–1252, 2021, ISSN: 19410107. DOI: 10.1109/TPEL.2020.3011470.
- [16] J. Everts, F. Krismer, J. Van Den Keybus, J. Driesen, and J. W. Kolar, "Charge-based ZVS soft switching analysis of a single-stage dual active bridge AC-DC converter," *2013 IEEE Energy Conversion Congress and Exposition, ECCE 2013*, pp. 4820–4829, 2013. DOI: 10.1109/ECCE.2013.6647349.
- [17] F. Sommer, N. Menger, T. Merz, and M. Hiller, "Accurate Time Domain Zero Voltage Switching Analysis of a Dual Active Bridge with Triple Phase Shift," *2021 23rd European Conference on Power Electronics and Applications, EPE 2021 ECCE Europe*, pp. 1–9, 2021.
- [18] C. P. Steinmetz, "On the law of hysteresis (part ii.) and other phenomena of the magnetic circuit," *Transactions of the American Institute of Electrical Engineers*, vol. 9, no. 1, pp. 619–758, 1892, ISSN: 00963860. DOI: 10.1109/T-AIEE.1892.5570469.
- [19] K. Venkatachalam, C. R. Sullivan, T. Abdallah, and H. Tacca, "Accurate prediction of ferrite core loss with nonsinusoidal waveforms using only steinmetz parameters," in *Proceedings of the IEEE Workshop on Computers in Power Electronics, COMPEL*, vol. 2002-Janua, 2002, pp. 36–41, ISBN: 0780375548. DOI: 10.1109/CIPE.2002.1196712.
- [20] F. Stamer, R. Schwendemann, and M. Hiller, "A multi-dimensional full automatic power semiconductor test bench for accurate semiconductor loss calculation," *PCIM Europe Conference Proceedings*, no. May, pp. 1411–1418, 2019, ISSN: 21913358.
- [21] TDK Electronics AG, "Ferrites and accessories - PM 74/59 - Core and accessories," 2019.
- [22] J. Mühlethaler, J. Biela, J. W. Kolar, and A. Ecklebe, "Improved core-loss calculation for magnetic components employed in power electronic systems," *IEEE Transactions on Power Electronics*, vol. 27, no. 2, pp. 964–973, 2012, ISSN: 08858993. DOI: 10.1109/TPEL.2011.2162252.
- [23] Hottinger Bruel und Kjaer GmbH, "GEN-Serie - GN310B (GN311B)," 2021.
- [24] Signaltec GmbH, "CT High Precision Current Transducers Current Transducers - Specifications," *LEM International SA*, pp. 1–30, 2022.